

Charge self-consistent density functional theory plus ghost rotationally invariant slave-boson theory for correlated materials

Tsung-Han Lee ^{1,2,*} Corey Melnick ³ Ran Adler ¹ Xue Sun,¹ Yongxin Yao ⁴ Nicola Lanatà ^{5,6} and Gabriel Kotliar^{1,3}

¹*Physics and Astronomy Department, Rutgers University, Piscataway, New Jersey 08854, USA*

²*Department of Physics, National Chung Cheng University, Chiayi 62102, Taiwan*

³*Condensed Matter Physics and Materials Science Department, Brookhaven National Laboratory, Upton, New York 11973, USA*

⁴*Ames National Laboratory and Iowa State University, Ames, Iowa 50011, USA*

⁵*School of Physics and Astronomy, Rochester Institute of Technology, 84 Lomb Memorial Drive, Rochester, New York 14623, USA*

⁶*Center for Computational Quantum Physics, Flatiron Institute, New York, New York 10010, USA*



(Received 13 June 2024; revised 2 September 2024; accepted 5 September 2024; published 13 September 2024)

We present a charge self-consistent density functional theory combined with the ghost rotationally invariant slave-boson (DFT+gRISB) formalism for studying correlated materials. This method is applied to SrVO₃ and NiO, representing prototypical correlated metals and charge-transfer insulators. For SrVO₃, we demonstrate that DFT+gRISB yields an accurate equilibrium volume and effective mass close to experimentally observed values. Regarding NiO, DFT+gRISB enables the simultaneous description of charge-transfer and Mott-Hubbard bands, significantly enhancing the accuracy of the original DFT+RISB approach. Furthermore, the calculated equilibrium volume and spectral function reasonably agree with experimental observations.

DOI: [10.1103/PhysRevB.110.115126](https://doi.org/10.1103/PhysRevB.110.115126)

I. INTRODUCTION

Simulating strongly correlated materials from first principles remains one of the most formidable challenges in condensed matter physics. The complexities arise from the intricate interplay among electronic charge, spin, and orbital degrees of freedom, as well as the electron's dual localization and itinerancy character in these materials, driven by strong local Coulomb interactions. This necessitates the use of quantum many-body techniques that go beyond standard *ab initio* density functional theory (DFT) [1,2] for their description.

The combination of DFT with dynamical mean-field theory (DFT+DMFT) has been extraordinarily successful in addressing this challenge [3,4]. The DMFT, as the first example of a quantum embedding approach, maps the interacting lattice to an auxiliary quantum impurity model with self-consistently determined bath orbitals [5], allowing an accurate description of the local correlation physics. Moreover, the DFT+DMFT has been extended to charge self-consistency deriving from a functional formulation [6,7]. The method requires a suitable selection of a correlated set of orbitals [8–12], the value of the interaction parameters [13,14], a suitable double-counting correction [14–16], and accurate impurity solvers [17,18]. This framework is now well developed, and comparisons between experiments and theory have revealed new physics in many correlated materials, shedding light on phenomena such as Mott localization [19–22], Hund's physics [23–28], and the valence fluctuations in correlated systems [29–31]. Nevertheless, the approach is computationally demanding and sometimes suffers from the so-called sign

problem in the quantum Monte Carlo solver with sizable off-diagonal hybridizations [17].

Another approach starts from the Gutzwiller approximation (GA) [32–40] and equivalently rotationally invariant slave-boson (RISB) method [41,42], and their combination with DFT [42–50]. These methods, realized as quantum embedding approaches [50,51], similar to DMFT, map the lattice problem onto an embedded impurity model and are connected to other quantum embedding concepts [50–54]. The RISB framework can capture local Mott, Hund's, and valence fluctuation physics [39,42,46,49,50], at a lower computational cost compared to DMFT. However, it sometimes suffers from insufficient accuracy, particularly failing to capture the interplay between the Mott physics and charge fluctuations [55,56].

The ghost rotationally invariant slave-boson (gRISB) method was recently introduced to overcome these limitations, expanding the RISB variational space by employing auxiliary ghost fermionic degrees of freedom [55,57,58]. Studies have shown that gRISB, even with a small number of ghost orbitals, consistently achieves ground-state and spectral properties that closely align with DMFT, across both single- and multi-orbital Hubbard models [55,57,59–62]. Additionally, numerical evidence indicates that the accuracy of gRISB approaches that of DMFT solutions as the number of ghost bath orbitals is increased [59,60,62,63]. This accuracy was confirmed through direct comparisons with DMFT, using exact diagonalization as an impurity solver and discretized hybridization functions [64]. Moreover, the gRISB requires the calculation of only the ground-state single-particle density matrix of the embedding Hamiltonian, avoiding the need to compute dynamic quantities of the impurity model, making it computationally efficient. The gRISB also does not require a bath fitting procedure and can be seamlessly combined with the density matrix renormalization group (DMRG) solvers

*Contact author: tsunghan@ccu.edu.tw

[62,65–67] and machine learning methods [68,69]. These features position gRISB as a promising approach warranting further investigation, particularly in combination with DFT.

In this work, we present a charge self-consistent DFT plus gRISB (DFT+gRISB) formalism to simulate correlated materials. We apply DFT+gRISB to SrVO₃ and NiO, representing correlated metal and charge-transfer insulator systems, respectively, and compare the results with DFT+DMFT. For SrVO₃, we demonstrate that DFT+gRISB yields reliable total energy and mass renormalization, in good agreement with experiments and DFT+DMFT studies, significantly improving upon the original RISB approach. For NiO, we show that DFT+gRISB provides a consistent description of the charge-transfer insulator, consistent with experimental and DFT+DMFT studies, while DFT+RISB falsely predicts a metallic solution for NiO. The DFT+gRISB total energy is also in good agreement with DFT+DMFT. Finally, we demonstrate the applicability of the DMRG solver within the gRISB framework, allowing for accurate results, including full five *d* orbitals.

II. METHOD

In this section, we discuss the formalism of the charge self-consistent DFT+gRISB approach and the implementation of our DFT+gRISB framework.

A. Formalism

The DFT+gRISB functional is encoded in a Lagrange function [6,50] represented as follows:

$$\begin{aligned} \mathcal{L}_N^{\text{DFT+gRISB}}[\rho(\mathbf{r}), \mathcal{J}(\mathbf{r}), \mu, V_i^0, N_i^0] \\ = \mathcal{L}_{\text{gRISB}}[\mathcal{J}(\mathbf{r}), \mu] \\ - \int d\mathbf{r} \rho(\mathbf{r})\mathcal{J}(\mathbf{r}) + E_{\text{Hxc}}[\rho(\mathbf{r})] + E_{\text{ion-ion}} + E_{\text{ion}}[\rho(\mathbf{r})] \\ + \sum_i E_{\text{dc}}^i[N_i^0] - \sum_i V_i^0 N_i^0 + \mu \left(N + \sum_i m_i \right), \quad (1) \end{aligned}$$

where N is the total number of electrons in the system, determined by the charge-neutrality condition, μ is the chemical potential, $\rho(\mathbf{r})$ is the electron density, $\mathcal{J}(\mathbf{r})$ is the corresponding constraining field, E_{Hxc} is the Hartree exchange-correlation functional, $E_{\text{ion-ion}}$ is the ion-ion energy, E_{ion} is the ionic potential, $E_{\text{dc}}^i[N_i^0] = \frac{U_i}{2} N_i^0 (N_i^0 - 1) - \frac{J_i}{2} N_i^0 (\frac{N_i^0}{2} - 1)$ is the double-counting energy functional associated with the i th impurity [14,15], N_i^0 is the corresponding occupancy, V_i^0 is the corresponding potential, and U_i and J_i is the corresponding Coulomb interaction and Hund's coupling interaction, respectively.

The term $\mathcal{L}_{\text{gRISB}}$ is the gRISB Lagrange function associated with the following many-body Kohn-Sham-Hubbard reference system, expressed in second quantization as follows:

$$\begin{aligned} \hat{H}_{\text{KSH}} = \int dx \hat{\Psi}^\dagger(x) \hat{P}[-\hat{\nabla}^2 + \mathcal{J}(\hat{x}) - \mu] \hat{P} \hat{\Psi}(x) \\ + \sum_{\mathbf{R}, i} \left(\hat{H}_i^{\text{int}}[c_{\mathbf{R}i\alpha}^\dagger, c_{\mathbf{R}i\alpha}] + V_i^0 \sum_{\alpha} c_{\mathbf{R}i\alpha}^\dagger c_{\mathbf{R}i\alpha} \right), \quad (2) \end{aligned}$$

where $x = (\mathbf{r}, \sigma)$, σ is the spin variable, \mathbf{r} is the position variable, $\int dx$ indicates both the sum over σ and the integral over \mathbf{r} , ∇^2 is the Laplacian, $\hat{\Psi}(x)$ is the Fermionic field operator, \hat{P} is the projector over a generic computational basis span, e.g., the Kohn-Sham band basis or linearized augmented plane-wave basis [70], and:

$$c_{\mathbf{R}i\alpha} = \int dx \phi_{\mathbf{R}i\alpha}^*(x) \hat{\Psi}(x) \quad (3)$$

$$\phi_{\mathbf{R}i\alpha}(\mathbf{r}) = \mathcal{N}^{-1} \sum_{\mathbf{k}} e^{-i\mathbf{k}\mathbf{R}} \phi_{\mathbf{k}i\alpha}(x) \quad (4)$$

are the annihilation operators associated with the corresponding correlated degrees of freedom, where \mathbf{R} is the unit cell label, \mathbf{k} is the momentum, and \mathcal{N} is the total number of unit cells in the system. The correlated orbital function is denoted by $\phi_{\mathbf{R}i\alpha}(x)$, where $\alpha = 1, \dots, \nu_i$ encodes both the orbital degrees of freedom and the spin.

The Lagrangian $\mathcal{L}_{\text{gRISB}}$ can be formally expressed as follows:

$$\begin{aligned} \mathcal{L}_{\text{gRISB}}[\mathcal{J}(\mathbf{r}), \mu] \\ = -\frac{T}{\mathcal{N}} \sum_{\omega} \text{Tr} \log[i\omega - H^{\text{qp}}] \\ + \mathcal{N} \sum_i [\langle \Phi_i | \hat{H}^{\text{emb}} | \Phi_i \rangle + E_i^c (1 - \langle \Phi_i | \Phi_i \rangle)] \\ - \mathcal{N} \sum_i \left[\sum_{ab} ([\lambda_i]_{ab} + [\lambda_i^c]_{ab}) [\Delta_i]_{ab} \right. \\ \left. + \mathcal{N} \sum_{a\alpha} ([D_i]_{a\alpha} [R_i]_{\alpha a} [\Delta_i (1 - \Delta_i)]_{ca}^{\frac{1}{2}} + \text{c.c.}) \right], \quad (5) \end{aligned}$$

where H^{qp} is the single-particle matrix representation of the so-called quasiparticle Hamiltonian:

$$\begin{aligned} \hat{H}^{\text{qp}} = \int dx \hat{\Psi}_u^\dagger(x) \hat{P}[-\hat{\nabla}^2 + \mathcal{J}(\hat{x}) - \mu] \hat{P} \hat{\Psi}_u(x) \\ + \int dx \hat{\Psi}_c^\dagger(x) \hat{P}[-\hat{\nabla}^2 + \mathcal{J}(\hat{x}) - \mu] \hat{P} \hat{\Psi}_c(x) \\ + \left(\int dx \hat{\Psi}_c^\dagger(x) \hat{P}[-\hat{\nabla}^2 + \mathcal{J}(\hat{x})] \hat{P} \hat{\Psi}_u(x) \right. \\ \left. + \text{H.c.} \right) + \sum_{\mathbf{k}i} \sum_{ab} [\lambda_i - \mathcal{E}_i^{\text{qp}}]_{ab} f_{\mathbf{k}i\alpha}^\dagger f_{\mathbf{k}i\beta} \quad (6) \end{aligned}$$

for a given computational basis projector \hat{P} and correlated orbital wave function $\phi_{\mathbf{R}i\alpha}(x)$, and the local correlated part of the H^{qp} has the form:

$$[\mathcal{E}_i^{\text{qp}}]_{ab} = \sum_{\alpha\beta} [R_i]_{a\alpha} [\mathcal{E}_i^{\text{loc}}]_{\alpha\beta} [R_i^\dagger]_{\beta b} \quad (7)$$

with

$$[\mathcal{E}_i^{\text{loc}}]_{\alpha\beta} = \frac{1}{\mathcal{N}} \sum_{\mathbf{k}} \langle \phi_{\mathbf{k}i\alpha} | -\hat{\nabla}^2 + \mathcal{J}(\hat{x}) | \phi_{\mathbf{k}i\beta} \rangle. \quad (8)$$

The matrix elements of R_i and λ_i are the so-called renormalization coefficients of the quasiparticle Hamiltonian, Δ_i is the quasiparticle single-particle density matrix. The $\hat{\Psi}_u(x)$ and $\hat{\Psi}_c$

is the uncorrelated and correlated part of the field operator, respectively, defined as follows:

$$\hat{\Psi}_u(x) = \left[\hat{I} - \sum_{\mathbf{k}\alpha} |\phi_{\mathbf{k}\alpha}\rangle \langle \phi_{\mathbf{k}\alpha}| \right] \hat{\Psi}(x) \quad (9)$$

$$\hat{\Psi}_c(x) = \sum_{\mathbf{k}\alpha} f_{\mathbf{k}\alpha} \sum_{\alpha} [R_i^\dagger]_{\alpha\alpha} \phi_{\mathbf{k}\alpha}(x), \quad (10)$$

where \hat{I} is the identity operator, $a = 1, \dots, Bv_i$, with B controlling the accuracy of the gRISB method, and $f_{\mathbf{k}\alpha}$ are the so-called quasiparticle annihilation operators. We have also introduced the so-called embedding Hamiltonian of the i th impurity:

$$\begin{aligned} \hat{H}_i^{\text{emb}} &= \hat{H}_i^{\text{int}}[c_{i\alpha}^\dagger, c_{i\alpha}] + V_i^0 \sum_{\alpha} c_{i\alpha}^\dagger c_{i\alpha} \\ &+ \sum_{\alpha\beta} [\mathcal{E}_i^{\text{loc}}]_{\alpha\beta} c_{i\alpha}^\dagger c_{i\beta} + \sum_{\alpha\alpha} ([D_i]_{\alpha\alpha} c_{i\alpha}^\dagger b_{i\alpha} + \text{c.c.}) \\ &+ \sum_{ab} [\lambda_i^c]_{ab} b_{ib} b_{ia}^\dagger. \end{aligned} \quad (11)$$

The matrix elements of D_i and λ_i^c is the hybridization and bath coupling constants, respectively, $|\Phi_i\rangle$ is the ground state of \hat{H}_i^{emb} , E_i^c is a Lagrange multiplier enforcing the normalization of $|\Phi_i\rangle$, and $c_{i\alpha}$, $b_{i\alpha}$ are the impurity and bath Fermionic annihilation operators, respectively. The number of spin orbitals in the bath is $N_{b,i} = Bv_i$.

The charge neutrality is enforced by the chemical potential μ at quasiparticle occupancy $N + \sum_i m_i$, where $m_i = (Bv_i - v_i)/2$. The reason for this additional term m_i is to enforce the physical occupancy to be at the total physical valence number N , where the quasiparticle occupancy and the physical occupancy differs by a number $\sum_i m_i$ [55,58]. The λ_i and λ_i^c can also be viewed as the Lagrange multiplier enforcing the gRISB constraints, and D_i is a Lagrange multiplier enforcing the structure of the $[R_i]_{\alpha\alpha} = \langle \Phi_i | c_{i\alpha}^\dagger b_{ib} | \Phi_i \rangle [\Delta_i(1 - \Delta_i)]_{ba}^{-\frac{1}{2}}$ matrix [41].

The stationary condition of the DFT+gRISB functional leads to the following saddle-point equations:

$$\mathcal{J}(\mathbf{r}) = \frac{\delta H_{\text{Hxc}}^{\text{LDA}}[\rho(\mathbf{r})]}{\delta \rho(\mathbf{r})} + \frac{\delta E_{\text{ion}}[\rho(\mathbf{r})]}{\delta \rho(\mathbf{r})}, \quad (12)$$

$$\frac{1}{\mathcal{N}} \sum_{\mathbf{k}} \langle f_{\mathbf{k}\alpha}^\dagger f_{\mathbf{k}\beta} \rangle_0 = [\Delta_i]_{\alpha\beta}, \quad (13)$$

$$\begin{aligned} \rho(\mathbf{r}) &= \langle \hat{\Psi}_u^\dagger(\mathbf{r}) \hat{\Psi}_u(\mathbf{r}) \rangle_0 + \langle \hat{\Psi}_c^\dagger(\mathbf{r}) \hat{\Psi}_c(\mathbf{r}) \rangle_0 \\ &+ (\langle \hat{\Psi}_c^\dagger(\mathbf{r}) \hat{\Psi}_u(\mathbf{r}) \rangle_0 + \text{H.c.}) + \frac{1}{\mathcal{N}} \sum_i \sum_{\mathbf{k}} \sum_{\alpha\beta} \phi_{\mathbf{k}\alpha}^*(\mathbf{r}) \\ &\times \left(\langle \Phi_i | c_{i\alpha}^\dagger c_{i\beta} | \Phi_i \rangle - \sum_{ab} [R_i^\dagger]_{\alpha a} [\Delta_i]_{ab} [R_i]_{b\beta} \right) \phi_{\mathbf{k}\beta}(\mathbf{r}), \end{aligned} \quad (14)$$

$$\begin{aligned} &\int dx \frac{1}{\mathcal{N}} \sum_{\mathbf{k}} \sum_{b\beta} \sum_{i'} \phi_{\mathbf{k}\alpha}^*(x) \hat{P} \\ &\times [-\nabla^2 + J(\hat{x}) - \mu] \hat{P} \phi_{\mathbf{k}\beta}(x) [R_i^\dagger]_{\beta b} \langle f_{\mathbf{k}\alpha}^\dagger f_{\mathbf{k}\beta} \rangle_0 \end{aligned}$$

$$\begin{aligned} &+ \int dx \frac{1}{\mathcal{N}} \sum_{\mathbf{k}} \phi_{\mathbf{k}\alpha}^*(x) \hat{P} [-\nabla^2 + J(\hat{x})] \hat{P} \langle f_{\mathbf{k}\alpha}^\dagger \hat{\Psi}_u(x) \rangle_T \\ &= \sum_c [D_i]_{c\alpha} [\Delta_i(1 - \Delta_i)]_{dc}^{\frac{1}{2}}, \end{aligned} \quad (15)$$

$$\int dx \langle \hat{\Psi}_u^\dagger(x) \hat{\Psi}_u(x) \rangle_0 + \langle \hat{\Psi}_c^\dagger(x) \hat{\Psi}_c(x) \rangle_0 = N + \sum_i m_i, \quad (16)$$

$$\sum_{cd\alpha} \frac{\partial}{\partial d_{i,s}} ([\Delta_i(1 - \Delta_i)]_{cd}^{\frac{1}{2}} [D_i]_{d\alpha} [R_i]_{c\alpha} + \text{c.c.}) + l_{i,s} + l_{i,s}^c = 0, \quad (17)$$

$$\hat{H}_i^{\text{emb}} |\Phi_i\rangle = E_i^c |\Phi_i\rangle, \quad (18)$$

$$\langle \Phi_i | c_{i\alpha}^\dagger b_{i\alpha} | \Phi_i \rangle - \sum_c [\Delta_i(1 - \Delta_i)]_{dc}^{\frac{1}{2}} [R_i]_{c\alpha} = 0, \quad (19)$$

$$\langle \Phi_i | b_{ib} b_{i\alpha}^\dagger | \Phi_i \rangle - [\Delta_i]_{ab} = 0, \quad (20)$$

where $\langle \dots \rangle_0$ denotes the average over the ground state of H_i^{emb} , and we introduced the following parametrization of the matrices:

$$[\Delta_i]_{ab} = \sum_s d_{i,s} [h_{i,s}]_{ab} \quad (21)$$

$$[\lambda_i]_{ab} = \sum_s l_{i,s} [h_{i,s}]_{ab} \quad (22)$$

$$[\lambda_i^c]_{ab} = \sum_s l_{i,s}^c [h_{i,s}]_{ab}, \quad (23)$$

where $h_{i,s}$ is an orthonormal basis of the Hermitian matrices [42]. Equation (12) gives rise to the Kohn-Sham potential, and Eq. (14) is the DFT+gRISB charge density, where the local quasiparticle contribution to the density is subtracted and replaced with the contribution from the local physical density matrix [45]. The chemical potential is determined from Eq. (16). The other equations are the standard gRISB equations for model Hamiltonian [55,57,58,61,62]. The detailed algorithm for solving these equations will be discussed in the next section.

With the converged R_i and λ_i , one can compute the Green's function as follows:

$$\begin{aligned} [G_i(\mathbf{k}, \omega)]_{\alpha\beta} &= \sum_{ab} [R_i^\dagger]_{\alpha a} \langle 0 | f_{\mathbf{k}\alpha} \frac{1}{\omega + i\eta - \hat{H}^{\text{qp}} + \mu} f_{\mathbf{k}\beta}^\dagger | 0 \rangle [R_i]_{b\beta}, \end{aligned} \quad (24)$$

where $|0\rangle$ is the vacuum. Equation (24) holds because the \hat{H}^{qp} is a single-particle Hamiltonian. The spectral function is calculated from $A_i(\mathbf{k}, \omega) = -\text{Im}G_i(\mathbf{k}, \omega)/\pi$, and we use a broadening factor of $\eta = 0.05$ eV.

The self-energy can be determined from the Dyson equation:

$$\begin{aligned} [\Sigma_i(\omega)]_{\alpha\beta} &= \langle \phi_{\mathbf{k}\alpha} | \omega + i0^+ - (\hat{\nabla}^2 - J(\hat{x}) - \mu) | \phi_{\mathbf{k}\beta} \rangle \\ &- [G_i^{-1}(\mathbf{k}, \omega)]_{\alpha\beta}. \end{aligned} \quad (25)$$

Note that the self-energy is momentum independent in gRISB, i.e., $\Sigma_i(\mathbf{k}, \omega) = \Sigma_i(\omega)$. The quasiparticle renormalization weight is determined from:

$$\mathbf{Z} = \left[1 - \left. \frac{\partial \text{Re}\Sigma(\omega)}{\partial \omega} \right|_{\omega \rightarrow 0} \right]^{-1}. \quad (26)$$

The expectation value of a generic local operator \hat{O} is computed from the embedding wave function:

$$\langle \hat{O} \rangle = \langle \Phi_i | \hat{O} [c_{i\alpha}^\dagger, c_{i\alpha}] | \Phi_i \rangle. \quad (27)$$

B. Implementation

Our implementation closely follows the previous works [42,50]. We utilize WIEN2K for the DFT part of the calculation [71]. The projector to the correlated orbitals is constructed from the atomic orbital modified from the density functional theory plus embedded dynamical mean-field theory (DFT+eDMFT) code [12,72]. The temperature broadening method is utilized for the Brillouin zone integration with a broadening factor of 0.02 eV. We utilized the local density approximation (LDA) functional in our calculations; however, our formalism is applicable to any exchange-correlation functional. We use 5000 k points and 2000 k points for the NiO and SrVO₃, respectively, and the RK_{max} is set to 7. The energy window for constructing the low-energy Hubbard model is $[-10 \text{ eV to } 10 \text{ eV}]$. The fully localized limit (FFL) is used as our double-counting scheme [14–16], where the nominal valence occupancy is set to 8 and 2 for NiO and SrVO₃, respectively. We use the DMRG approach implemented in theBLOCK2 software, based on matrix product state formalism [73], to solve the ground-state wave function of the embedding Hamiltonian H^{emb} in Eq. (11). The bond dimension is set to 2000 in our DMRG calculations. For constructing our bath orbitals $b_{i\alpha}$ in Eq. (11), we utilize the gauge invariant nature of gRISB to fix the λ^c as a diagonal matrix to reduce the entanglement between the bath orbitals, see Appendix D. For the DFT+DMFT calculations, we utilize the DFT+eDMFT code with the same parameter setting as in the DFT+gRISB calculations, which provides a consistent benchmark between the DFT+DMFT and DFT+gRISB methods. The continuous-time quantum Monte Carlo solver is utilized with 10^9 Monte Carlo steps distributed over 200 CPUs, and the temperature is set to 100 K. For both methods, we treat all five d orbitals as correlated shells, and the interaction is of full Slater-Condon type [13,14].

The DFT+gRISB self-consistent equations are implemented as follows: (i) converge the DFT calculations to obtain the Kohn-Sham eigenvalue and eigenvectors, (ii) construct the projector from the Kohn-Sham eigenvector and the local atomic orbitals, (iii) solve the gRISB saddle-point equations Eqs. (13)–(20) with the Kohn-Sham eigenvalues and the projector, (iv) use the gRISB saddle-point solution to compute the new charge density from Eq. (14), (v) feedback the new charge density to DFT to update the new exchange-correlated potential [Eq. (12)] and go to step (i) until the charge density and total energy is converged. In our calculations, we set the total energy convergence criteria to 10^{-5} eV and the charge convergence criteria to 10^{-3} .

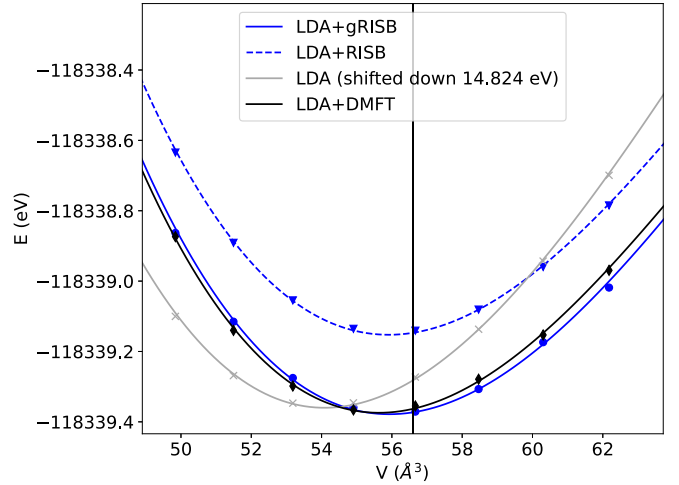


FIG. 1. Calculated energy volume curve with LDA, LDA+RISB, LDA+gRISB, and LDA+DMFT for SrVO₃ with $U = 10 \text{ eV}$ and $J = 1 \text{ eV}$. The experimental equilibrium volume is 56.61 \AA^3 [74]. The temperature in DMFT is $T = 100 \text{ K}$.

III. RESULTS

A. Applications to SrVO₃

In this section, we apply LDA+gRISB to SrVO₃ and investigate its total energy and electronic structures. This material has been studied extensively in the past decades and serves as an ideal material for benchmarking new approaches [9,16,75–90]. It has a cubic perovskite structure, and the main active orbitals around the Fermi level are in the $V-d_{t_{2g}}$ shell. The correlation effect is essential in SrVO₃, leading to significant renormalization of the bandwidth near the Fermi level.

We first discuss the total energy of the LDA+gRISB. Figure 1 summarized the total energy of LDA, LDA+RISB, LDA+gRISB, and LDA+DMFT as a function of the unit cell volume. First, we reproduce the known fact that LDA underestimates the equilibrium volume at 54 \AA^3 , while the experiment observed value is 56.61 \AA^3 . The LDA+RISB improves the equilibrium volume to 56 \AA^3 towards the experimental value, but the total energy is not consistent with LDA+DMFT at the quantitative level. On the other hand, LDA+gRISB with 15 bath orbitals significantly improves the total energy, in quantitative agreement with the LDA+DMFT results. The equilibrium volume of LDA+gRISB and LDA+DMFT is 56 \AA^3 and 55.8 \AA^3 , respectively.

We now discuss the electronic structure of SrVO₃. Figure 2 shows the momentum-resolved spectral function along the high-symmetry points and the orbital resolved density of states calculated from the LDA, LDA+RISB, LDA+gRISB, and LDA+DMFT approaches at the experimental equilibrium volume. The main characters around the Fermi level are the vanadium's t_{2g} orbitals. For the LDA calculation, the bandwidth of the t_{2g} bands is around 2 eV. When including the electronic correlation effects at the LDA+RISB level, we observe slight renormalization of the bandwidth by a factor around 0.8, which is inconsistent with the LDA+DMFT, where the renormalization factor is

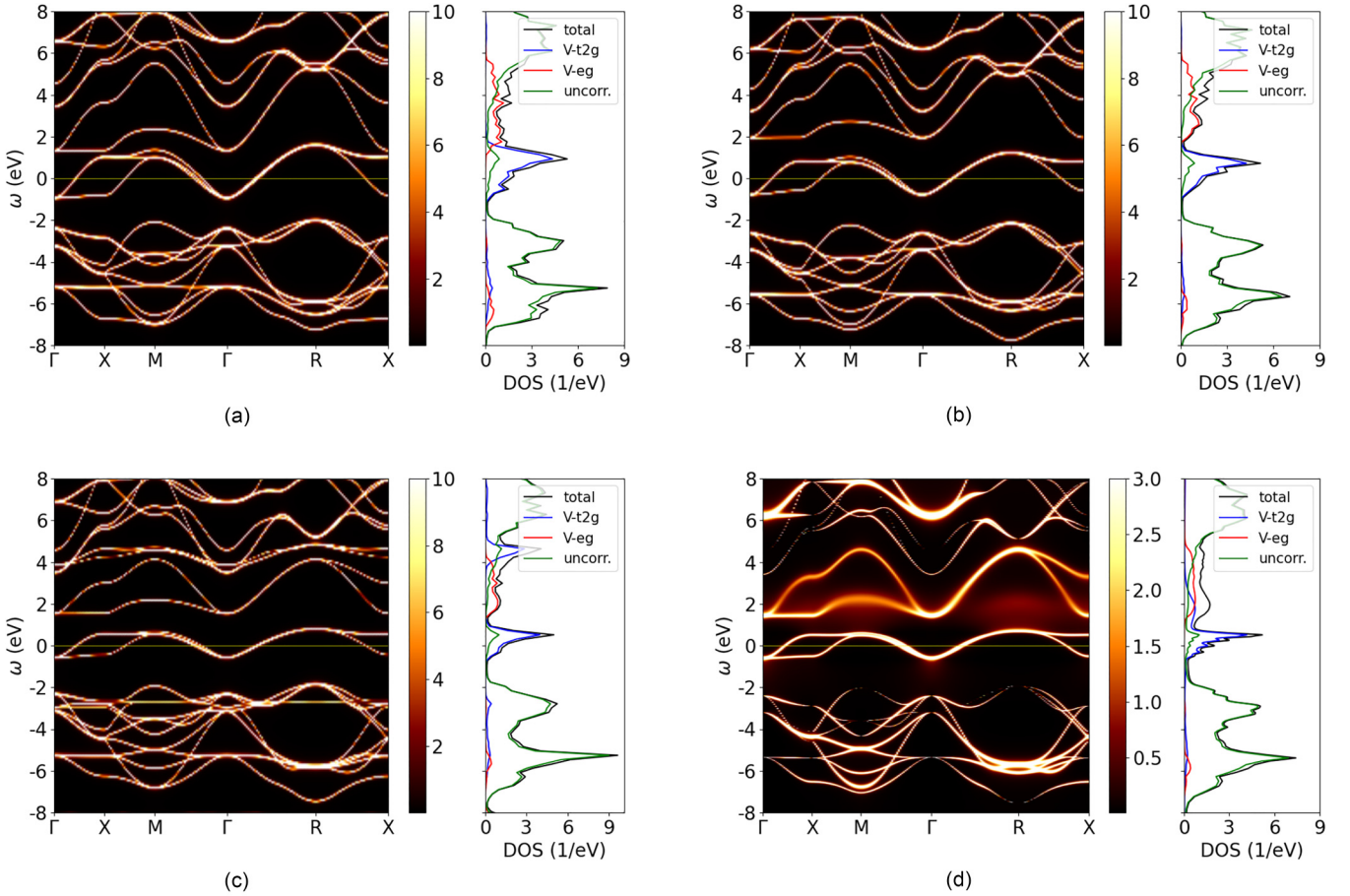


FIG. 2. The momentum-resolved spectral function $A(\mathbf{k}, \omega)$ and the orbital-resolved density of states for SrVO₃ with the (a) LDA, (b) LDA+RISB, (c) LDA+gRISB, and (d) LDA+DMFT approaches at the experimental equilibrium volume. The Coulomb parameters are $U = 10$ eV and $J = 1$ eV, and the temperature in DMFT is $T = 100$ K.

around 0.5. Moreover, the LDA+RISB electronic structure is almost identical to LDA, implying a weakly correlated metal that is inconsistent with LDA+DMFT. This inconsistency can be remedied by utilizing LDA+gRISB with 15 bath orbitals shown in Fig. 2(c). In the LDA+gRISB results, the t_{2g} bands are renormalized by a factor of 0.5 in agreement with LDA+DMFT. The improvement of the quasiparticle weight is originated from the enlarged variational space where the ghost orbitals introduced additional variational degrees of freedom, leading to more accurate descriptions to the ground state and spectral properties [57]. Moreover, the electronic structure closely resembles LDA+DMFT, except for the upper Hubbard band (around 4 eV) and the lower Hubbard band (around -3 eV) of the t_{2g} orbitals, which are approximated by coherent and less dispersive bands in LDA+gRISB. These less dispersive flat bands in LDA+gRISB mimic the incoherent Hubbard spectral weight in LDA+DMFT. However, since LDA+gRISB, with a small number of ghost orbitals, can only introduce a finite number of poles to the self-energy on the real axis [57,59], it cannot capture a finite scattering rate, which requires a branch cut on the real axis. As a result, these flat bands lack incoherent features and appear sharp in the spectra [57,59,62].

The total density of states calculated from LDA+RISB, LDA+gRISB, and LDA+DMFT at the equilibrium volume is

shown in Fig. 3, which are compared with the photoemission experiment [91]. The LDA+gRISB and LDA+DMFT density

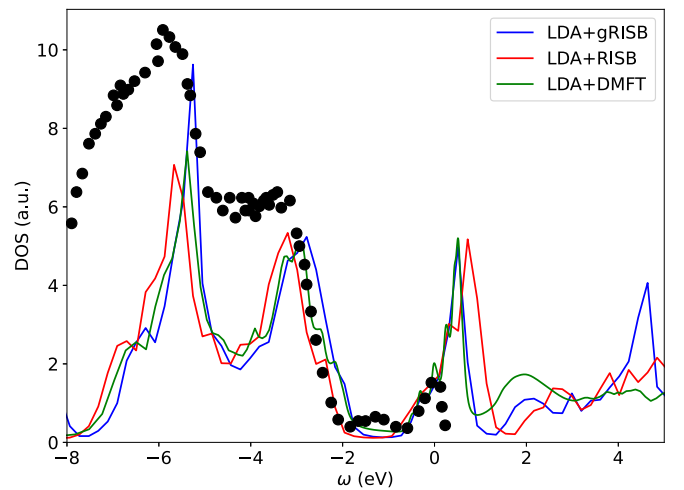


FIG. 3. Comparison of the LDA+RISB, LDA+gRISB, and LDA+DMFT SrVO₃ total density of states with the photoemission spectroscopy (the filled circles) [77]. The Coulomb interaction parameters are $U = 10$ eV and $J = 1$ eV. The temperature in DMFT is $T = 100$ K.

TABLE I. Quasiparticle weight Z and occupancy n for SrVO_3 calculated from LDA, LDA+RISB, and LDA+DMFT with Coulomb interaction parameters $U = 10$ eV and $J = 1$ eV at the experimental equilibrium volume.

	LDA	LDA+RISB	LDA+gRISB	LDA+DMFT
$Z_{t_{2g}}$	1	0.78	0.53	0.51
Z_{e_g}	1	0.89	0.75	0.78
$n_{t_{2g}}$	1.68	1.56	1.53	1.51
n_{e_g}	0.80	0.64	0.66	0.66

of states around the Fermi level are in good agreement with each other, while the upper Hubbard band in LDA+gRISB shows a coherent feature. All three methods capture the gap between -2 eV and 0.5 eV and the low-energy peaks, mainly attributed to the uncorrelated O and Sr atoms. Finally, we show the orbital-resolved quasiparticle weight Z and occupancy in Table I. The LDA+gRISB and LDA+DMFT values are in quantitative agreement. On the other hand, the LDA+RISB captures reliable occupancy, but the quasiparticle weight is overestimated.

B. Applications to NiO

We now apply LDA+gRISB to NiO, which is a prototypical charge-transfer insulator where the Ni- d_{e_g} orbitals hybridize with O- p to form the so-called charge-transfer band between the lower and the upper Hubbard band [93,94]. Moreover, the concept of the Zhang-Rice bound state forming by a hole on the O- p orbitals and the holes on the Ni- d orbitals has been introduced to explain the low-energy features of the photoemission spectra in this material [95–99]. The DFT+DMFT approach has been applied to NiO and reveals further insight into the electronic structure of this charge-transfer insulator as well as its properties with external pressure, doping, and the surface effects [97,100–107]. In this work, we focus on the paramagnetic phase of NiO and compare its total energy and electronic structure with the LDA+DMFT results.

The total energy as a function of the unit cell volume is shown in Fig. 4 for LDA, LDA+RISB, LDA+DMFT, and LDA+DMFT. The LDA significantly underestimates the unit cell volume around 16.6 \AA^3 compared to experimental volume 18.34 \AA^3 and fails to capture the experimentally observed insulating behavior, which is a well-known feature. The LDA+RISB also fails to produce an insulating solution with realistic Coulomb parameters, $U = 10$ eV and $J = 1$ eV [97,108], utilized in this work. Therefore, its total energy has a large 1 eV discrepancy compared to LDA+DMFT. On the other hand, LDA+gRISB captures the charge-transfer insulator behavior, significantly improving the total energy to a quantitative agreement with the LDA+DMFT values, with a difference of around 10 meV. This difference can be attributed to the finite temperature effect $T = 100$ K utilized in the LDA+DMFT calculations. The equilibrium volume of LDA+gRISB and LDA+DMFT is 18.09 \AA^3 and 18.03 \AA^3 , respectively

The DFT band structure and density of states are shown in Fig. 5(a). Without breaking the spin symmetry, DFT predicts a metallic solution, which is a known problem in DFT for

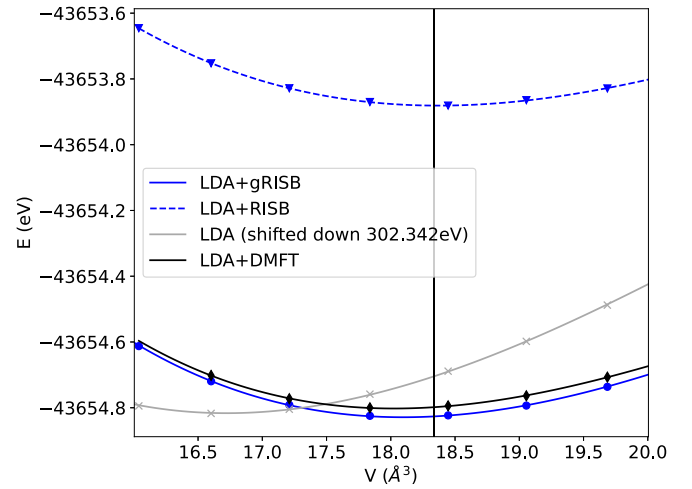


FIG. 4. Calculated energy volume curve with LDA, LDA+RISB, LDA+gRISB, and LDA+DMFT for NiO with Coulomb interaction parameters $U = 10$ eV and $J = 1$ eV. The experimental equilibrium volume is 18.34 \AA^3 [92]. The temperature in DMFT is $T = 100$ K.

transition metal oxides [109]. The bands around the Fermi level contain the O- p and Ni- d_{e_g} orbitals. The Ni- $d_{t_{2g}}$ orbitals are located below the Fermi level and are almost completely filled.

Next, we show the LDA+RISB momentum-resolved spectral function and density of states in Fig. 5(b). We utilize the constrained LDA Coulomb parameters $U = 10$ eV and $J = 1$ eV in our simulations [97,108]. In DFT+RISB, the correlation effects only slightly renormalized the bands around the Fermi level with $Z_{d_{e_g}} = 0.6$ and $Z_{d_{t_{2g}}} = 0.7$ and the system is far from the metal-insulator transition.

The LDA+gRISB momentum-resolved spectral function and density of states are shown in Fig. 5(c). Here, we use 17 bath orbitals in our LDA+gRISB calculations. The density of states shown in Fig. 5(c) demonstrate that LDA+gRISB accurately captures the charge-transfer insulating behavior in the density of states, where the Hubbard bands are opened in the Ni- d_{e_g} orbitals and charge-transfer band is observed around -1 eV with strong O- p and Ni- d hybridization. We also observe significant spectral weight around the valence band edge, which can be ascribed to the Zhang-Rice bound state [96–99]. These features are in good agreement with the LDA+DMFT results shown in Fig. 5(d) and the previous studies [97,100–102,105–107]. Moreover, the LDA+gRISB momentum-resolved spectral functions $A(\mathbf{k}, \omega)$ captures reliably the dispersive excitations compared to DFT+DMFT, except the incoherent broadening features, which cannot be described within the gRISB framework.

In Fig. 6, we compare the LDA+gRISB total density of states with LDA+DMFT and the photoemission bremsstrahlung isochromat spectroscopy (XPS/BIS) [91]. Our LDA+gRISB density of states captures the main features in the XPS/BIS spectrum, where the band gap is about 4 eV, and the heights of the peaks on the band edges are reasonably captured. On the other hand, LDA+DMFT has a band gap around 2 eV, smaller than the experimental band gap.

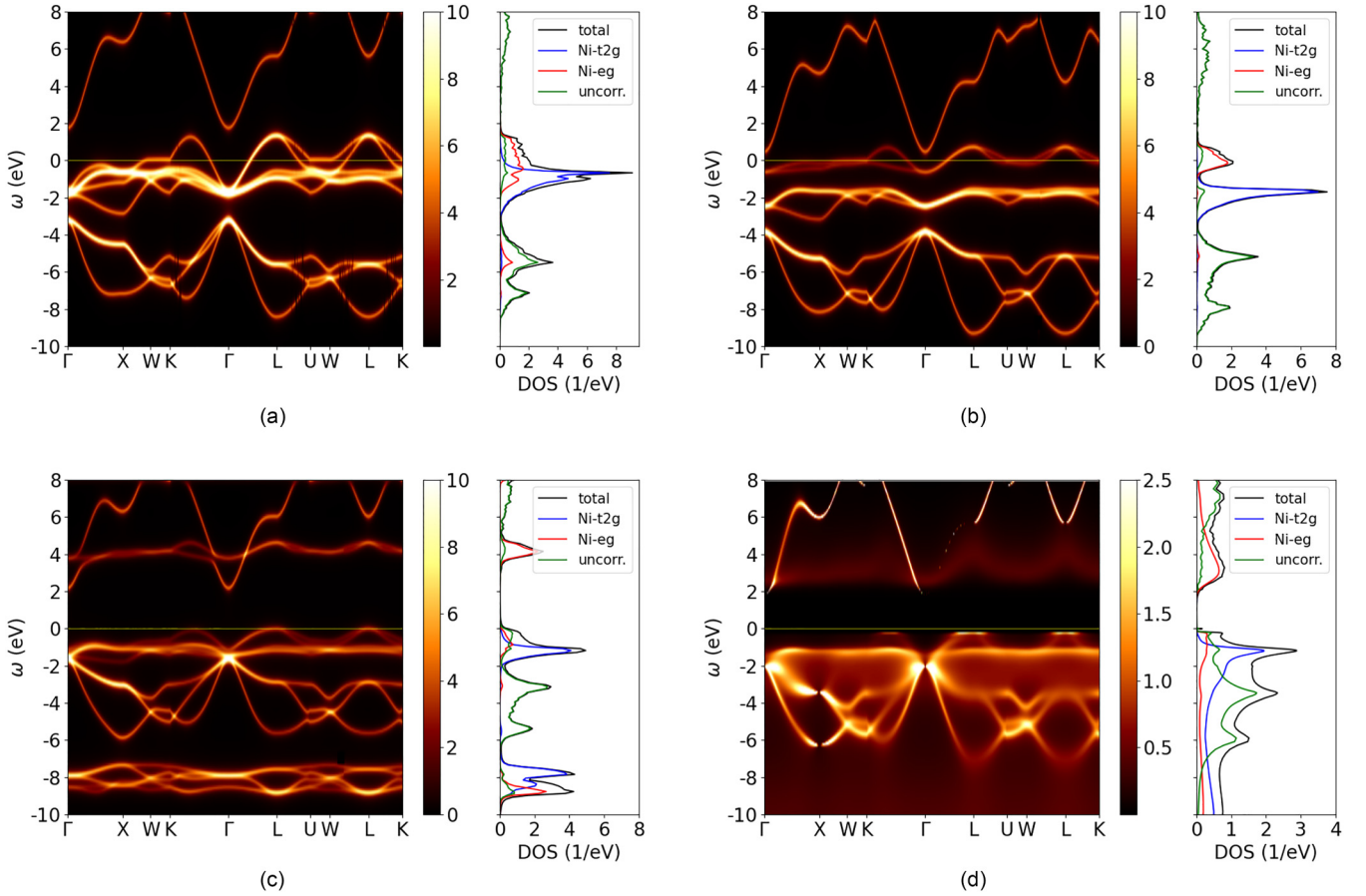


FIG. 5. The momentum-resolved spectral function $A(\mathbf{k}, \omega)$ and the orbital-resolved density of states for NiO with the (a) LDA, (b) LDA+RISB, (c) LDA+gRISB, and (d) LDA+DMFT approaches at the experimental equilibrium volume. The Coulomb parameters are $U = 10$ eV and $J = 1$ eV, and the temperature in DMFT is $T = 100$ K.

Finally, the orbital-resolved occupancy of different approaches is shown in Table II. The LDA+gRISB's occupancy is in good agreement with LDA+DMFT and improves the

LDA values. On the other hand, although LDA+RISB fails to capture the charge-transfer insulating solution, its occupancy is identical to the LDA+gRISB values and close to the LDA+DMFT values.

IV. CONCLUSIONS

We present a charge self-consistent DFT+gRISB approach to correlated materials and demonstrate its performance on two prototypical materials, SrVO₃ and NiO, representing the correlated metals and charge-transfer insulators. For SrVO₃, we show that DFT+gRISB reliably captures the total energy and effective mass compared to the experiment and DFT+DMFT values, significantly improving the original DFT+RISB approach. Furthermore, we show

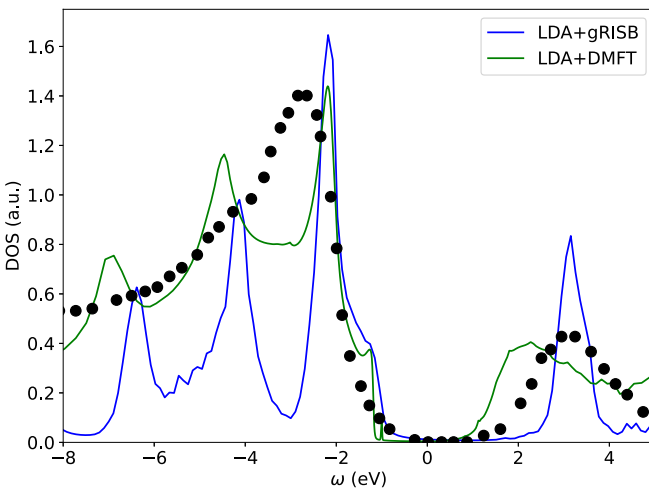


FIG. 6. Comparison of the LDA+gRISB and LDA+DMFT NiO total density of states with the photoemission and bremsstrahlung isochromat spectroscopy (the filled circles) [91]. The Coulomb interaction parameters are $U = 10$ eV and $J = 1$ eV. The temperature in DMFT is $T = 100$ K.

TABLE II. The occupancy n for NiO calculated from LDA, LDA+RISB, and LDA+DMFT with Coulomb interaction parameters $U = 10$ eV and $J = 1$ eV at the experimental equilibrium volume.

	LDA	LDA+RISB	LDA+gRISB	LDA+DMFT
n_{eg}	2.59	2.14	2.15	2.15
n_{t2g}	5.89	5.99	5.99	5.94

that DFT+gRISB provides a more accurate description of the electronic band structure for strongly correlated materials with a narrow quasiparticle peak and Hubbard bands compared to DFT+RISB. For NiO, DFT+gRISB captures the charge-transfer insulating behavior, with the charge-transfer band situated between the lower and upper Hubbard bands, significantly improving the DFT+RISB results, which falsely predicts a metallic state. The total density of states is in reasonable agreement with the photoemission spectrum. Moreover, our work demonstrates the applicability of DMRG as an impurity solver within the DFT+gRISB framework to reliably simulate correlated full five d -orbital systems.

Future work will extend the DFT+gRISB framework to study the two-particle response functions and interaction vertices [110,111], non-equilibrium dynamics [112–115], and to incorporate gRISB with Wannier-orbital-based projectors and other DFT frameworks and interfaces [116–129].

ACKNOWLEDGMENTS

T.-H.L. acknowledges discussions with H. Zhai on the block2 DMRG solver. T.-H.L., X.S., and G.K. were supported by the US Department of Energy, Office of Science, Office of Advanced Scientific Computing Research and Office of Basic Energy Sciences, Scientific Discovery through Advanced Computing (SciDAC) program under Award No. DE-SC0022198. C.M. and R.A. was supported by the US Department of Energy, Office of Basic Energy Sciences as part of the Computation Material Science Program. T.-H.L. gratefully acknowledges funding from the National Science and Technology Council (NSTC) of Taiwan under Grant No. NSTC 112-2112-M-194-007-MY3. N.L. gratefully acknowledges funding from the Simons Foundation (Grant No. 1030691, N.L.). The part of the work by Y.Y. was supported by the US Department of Energy (DOE), Office of Science, Basic Energy Sciences, Materials Science and Engineering Division, including the grant of computer time at the National Energy Research Scientific Computing Center (NERSC) in Berkeley, California. This part of research was performed at the Ames National Laboratory, which is operated for the US DOE by Iowa State University under Contract No. DE-AC02-07CH11358.

APPENDIX A: NiO RESULTS WITH DIFFERENT NUMBERS OF BATH ORBITALS

In the main text, we show the results of NiO with $N_b = 17$ bath orbitals in the LDA+gRISB calculations. Here, we present a comparison of the LDA+gRISB results with a smaller number of bath orbital $N_b = 15$, which is the minimum number of orbitals to capture the Mott insulator in LDA+gRISB with Hubbard bands. Figure 7 shows the total energy of NiO from the charge self-consistent LDA+gRISB calculations with $N_b = 15$ and $N_b = 17$ and from the charge self-consistent LDA+DMFT calculations. We observe that the $N_b = 15$ total energy deviates from the LDA+DMFT values, and increasing the number of orbitals to $N_b = 17$ improves the agreement with LDA+DMFT.

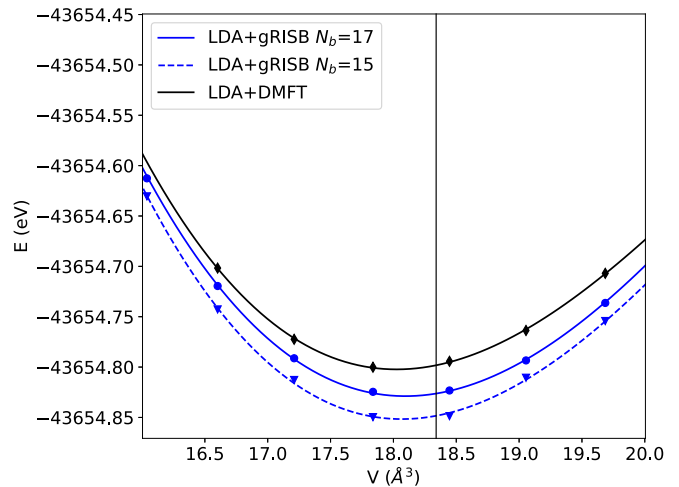


FIG. 7. Calculated energy volume curve with LDA+gRISB using $N_b = 15$ and $N_b = 17$ and LDA+DMFT for NiO with $U = 10$ eV and $J = 1$ eV. The temperature in DMFT is $T = 100$ K. The experimental equilibrium volume is 18.34 \AA^3 [92].

Figure 8 shows the momentum-resolved spectral function and density of states of NiO from the LDA+gRISB calculations with $N_b = 15$ bath orbitals. The LDA+gRISB spectral function with $N_b = 15$ is similar to the LDA+gRISB spectral function with $N_b = 17$ shown in Fig. 5(c), except for an additional band in the energy window between -6 eV and -4 eV, which is not consistent with LDA+DMFT. As shown in Fig. 5(c), increasing N_b to 17 improves the quality of the spectral functions.

APPENDIX B: ONE-SHOT AND CHARGE SELF-CONSISTENCY

In this section, we compare the one-shot (OS) LDA+gRISB results with the charge self-consistency (CSC) results presented in the main text to demonstrate the effect

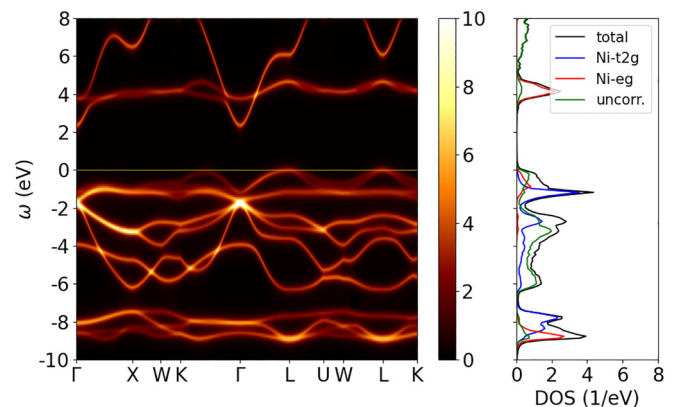


FIG. 8. The momentum-resolved spectral function $A(\mathbf{k}, \omega)$ and the orbital-resolved density of states for NiO with LDA+gRISB and $N_b = 15$ at the experimental equilibrium volume. The Coulomb parameters are $U = 10$ eV and $J = 1$ eV, and the temperature in DMFT is $T = 100$ K.

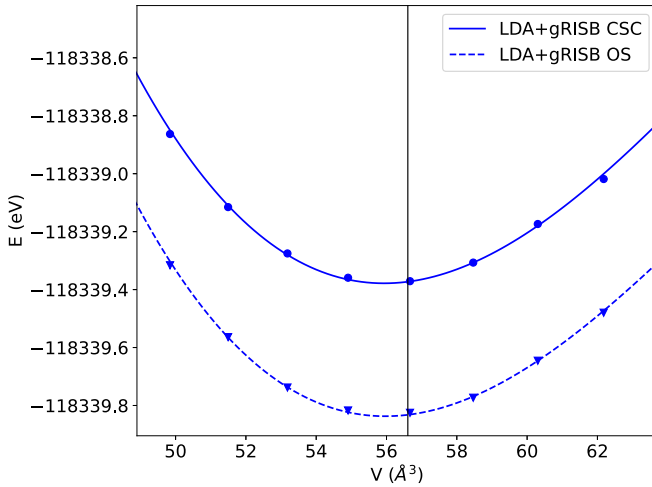


FIG. 9. Calculated energy volume curve with LDA+gRISB for SrVO₃ from the one-shot and charge self-consistent calculations with $U = 10$ eV and $J = 1$ eV. The temperature in DMFT is $T = 100$ K. The experimental equilibrium volume is 56.61 \AA^3 [74,92].

of CSC. We start from the total energy of SrVO₃ shown in Fig. 9. The CSC shifts the total energy upward. However, the OS equilibrium volume 56 \AA^3 is the same as the CSC value. The spectral function of the OS calculation is shown in Fig. 10. The overall feature of the OS spectral function is similar to the CSC spectral function in Fig. 2(c), except for the slightly wider band gap between the correlated t_{2g} band and the uncorrelated band around the energy window between 0.5 eV and -2 eV.

The comparison of the total energy of NiO between the OS and CSC calculations is shown in Fig. 11. The CSC shifts the total energy upward. However, the OS equilibrium volume 18.08 \AA^3 is close to the CSC value 18.09 \AA^3 . The OS momentum-resolved spectral function and density of states at the equilibrium volume is shown in Fig. 12. Compared to the CSC results shown in Fig. 5(c), we observed significant

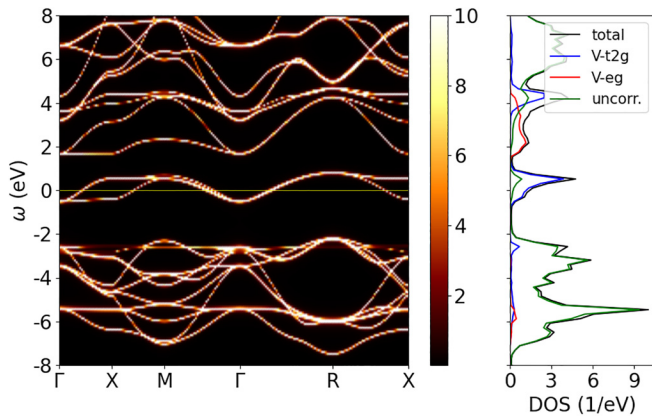


FIG. 10. The momentum-resolved spectral function $A(\mathbf{k}, \omega)$ and the orbital-resolved density of states for SrVO₃ with the one-shot LDA+gRISB calculation at the experimental equilibrium volume. The Coulomb parameters are $U = 10$ eV and $J = 1$ eV, and the temperature in DMFT is $T = 100$ K.

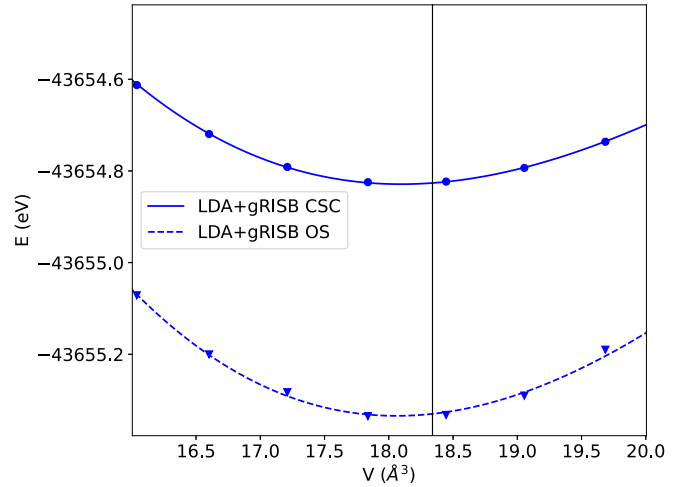


FIG. 11. Calculated energy volume curve with LDA+gRISB for NiO from the one-shot and charge-self-consistent calculations with $U = 10$ eV and $J = 1$ eV. The temperature in DMFT is $T = 100$ K. The experimental equilibrium volume is 18.34 \AA^3 [92].

modification of the band structure, especially the position of the upper Hubbard band around 5 eV (4 eV with CSC) and the lower Hubbard bands around -7 eV (-8 eV with CSC).

APPENDIX C: NiO RESULTS WITH DIFFERENT COULOMB INTERACTIONS

In this section, we compare the photoemission and bremsstrahlung isochromat spectroscopy with LDA+gRISB and LDA+DMFT with different Coulomb interaction parameters in Fig. 13. In general, we found that the incoherent features of the Hubbard band are more prominent in LDA+DMFT, leading to underestimations of the band gap. On the other hand, the Hubbard band is coherent in LDA+gRISB, resulting in larger band gaps for the considered Coulomb interactions.

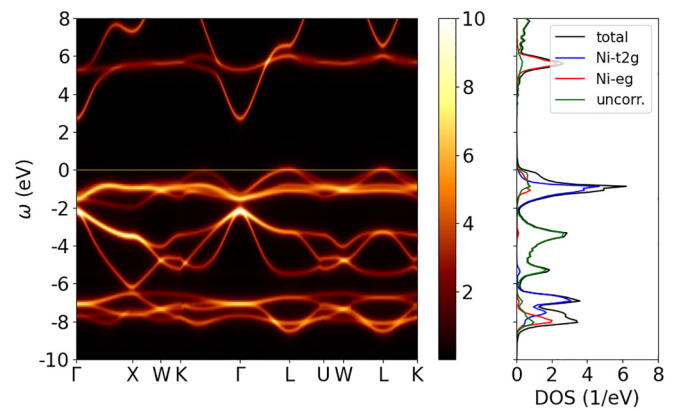


FIG. 12. The momentum-resolved spectral function $A(\mathbf{k}, \omega)$ and the orbital-resolved density of states for NiO with the one-shot LDA+gRISB calculations at the experimental equilibrium volume. The Coulomb parameters are $U = 10$ eV and $J = 1$ eV, and the temperature in DMFT is $T = 100$ K.

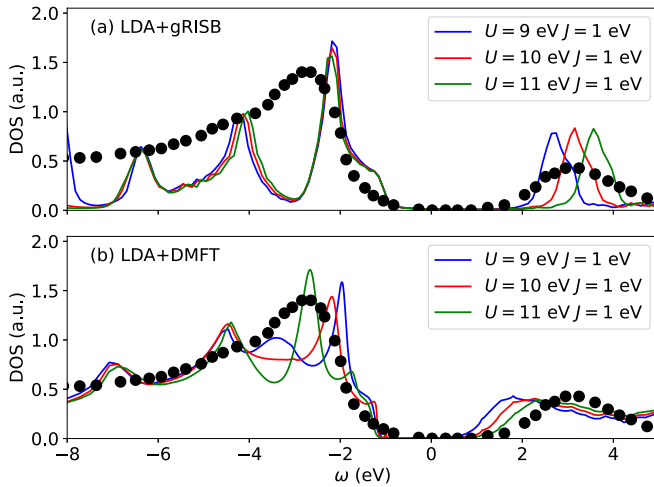


FIG. 13. Comparison of the DFT+gRISB and DFT+DMFT NiO total density of states with the Photoemission and bremsstrahlung isochromat spectroscopy (the filled circles) [91] with different Coulomb interactions. The temperature in DMFT is $T = 100$ K.

APPENDIX D: CONSTRUCTION OF THE BATH ORBITALS

The DMRG algorithm involves enumerating orbitals along an artificial one-dimensional chain to construct matrix product states and perform sweeping optimizations. Achieving high accuracy and efficiency depends on choosing a suitable orbital set that minimizes the entanglement between neighboring orbitals. To reduce the entanglement in the embedding Hamiltonian [Eq. (11)], we utilize the gauge invariance nature of gRISB to transform the λ_i^c matrix, describing the bath energy levels and hybridizations, to a diagonal matrix as follows [42,58]:

$$\lambda_i^c \rightarrow u_i^\dagger \lambda_i^c u_i \quad (\text{D1})$$

$$D_i \rightarrow u_i^\dagger D_i, \quad (\text{D2})$$

where u_i is a unitary gauge transformation matrix. This step can reduce the entanglement between the bath orbitals, lowering the required bond dimension to achieve better accuracy and efficiency.

- [1] P. Hohenberg and W. Kohn, Inhomogeneous electron gas, *Phys. Rev.* **136**, B864 (1964).
- [2] W. Kohn and L. J. Sham, Self-consistent equations including exchange and correlation effects, *Phys. Rev.* **140**, A1133 (1965).
- [3] V. I. Anisimov, A. I. Poteryaev, M. A. Korotin, A. O. Anokhin, and G. Kotliar, First-principles calculations of the electronic structure and spectra of strongly correlated systems: Dynamical mean-field theory, *J. Phys.: Condens. Matter* **9**, 7359 (1997).
- [4] A. I. Lichtenstein, M. I. Katsnelson, and G. Kotliar, Finite-temperature magnetism of transition metals: An *ab initio* dynamical mean-field theory, *Phys. Rev. Lett.* **87**, 067205 (2001).
- [5] A. Georges, G. Kotliar, W. Krauth, and M. J. Rozenberg, Dynamical mean-field theory of strongly correlated fermion systems and the limit of infinite dimensions, *Rev. Mod. Phys.* **68**, 13 (1996).
- [6] G. Kotliar, S. Y. Savrasov, K. Haule, V. S. Oudovenko, O. Parcollet, and C. A. Marianetti, Electronic structure calculations with dynamical mean-field theory, *Rev. Mod. Phys.* **78**, 865 (2006).
- [7] K. Held, Electronic structure calculations using dynamical mean field theory, *Adv. Phys.* **56**, 829 (2007).
- [8] S. Y. Savrasov and G. Kotliar, Spectral density functionals for electronic structure calculations, *Phys. Rev. B* **69**, 245101 (2004).
- [9] E. Pavarini, S. Biermann, A. Poteryaev, A. I. Lichtenstein, A. Georges, and O. K. Andersen, Mott transition and suppression of orbital fluctuations in orthorhombic $3d^1$ perovskites, *Phys. Rev. Lett.* **92**, 176403 (2004).
- [10] L. V. Pourovskii, B. Amadon, S. Biermann, and A. Georges, Self-consistency over the charge density in dynamical mean-field theory: A linear muffin-tin implementation and some physical implications, *Phys. Rev. B* **76**, 235101 (2007).
- [11] Dm. Korotin, A. V. Kozhevnikov, S. L. Skornyakov, I. Leonov, N. Binggeli, V. I. Anisimov, and G. Trimarchi, Construction and solution of a wannier-functions based Hamiltonian in the pseudopotential plane-wave framework for strongly correlated materials, *Eur. Phys. J. B* **65**, 91 (2008).
- [12] K. Haule, C.-H. Yee, and K. Kim, Dynamical mean-field theory within the full-potential methods: Electronic structure of CeIrIn₅, CeCoIn₅, and CeRhIn₅, *Phys. Rev. B* **81**, 195107 (2010).
- [13] V. I. Anisimov, I. V. Solovyev, M. A. Korotin, M. T. Czyżyk, and G. A. Sawatzky, Density-functional theory and NiO photoemission spectra, *Phys. Rev. B* **48**, 16929 (1993).
- [14] V. I. Anisimov, F. Aryasetiawan, and A. I. Lichtenstein, First-principles calculations of the electronic structure and spectra of strongly correlated systems: the LDA+ U method, *J. Phys.: Condens. Matter* **9**, 767 (1997).
- [15] M. T. Czyżyk and G. A. Sawatzky, Local-density functional and on-site correlations: The electronic structure of La₂CuO₄ and LaCuO₃, *Phys. Rev. B* **49**, 14211 (1994).
- [16] K. Haule, Exact double counting in combining the dynamical mean field theory and the density functional theory, *Phys. Rev. Lett.* **115**, 196403 (2015).
- [17] E. Gull, A. J. Millis, A. I. Lichtenstein, A. N. Rubtsov, M. Troyer, and P. Werner, Continuous-time monte carlo methods for quantum impurity models, *Rev. Mod. Phys.* **83**, 349 (2011).
- [18] R. Bulla, T. A. Costi, and T. Pruschke, Numerical renormalization group method for quantum impurity systems, *Rev. Mod. Phys.* **80**, 395 (2008).
- [19] A. Koga, N. Kawakami, T. M. Rice, and M. Sigrist, Orbital-selective Mott transitions in the degenerate Hubbard model, *Phys. Rev. Lett.* **92**, 216402 (2004).
- [20] L. de'Medici, A. Georges, and S. Biermann, Orbital-selective Mott transition in multiband systems: Slave-spin representation and dynamical mean-field theory, *Phys. Rev. B* **72**, 205124 (2005).

- [21] R. Yu and Q. Si, Orbital-selective Mott phase in multiorbital models for alkaline iron selenides $K_{1-x}Fe_{2-y}Se_2$, *Phys. Rev. Lett.* **110**, 146402 (2013).
- [22] X. Deng, K. M. Stadler, K. Haule, A. Weichselbaum, J. von Delft, and G. Kotliar, Signatures of Mottness and Hundness in archetypal correlated metals, *Nature Commun.* **10**, 2721 (2019).
- [23] A. Georges, L. de' Medici, and J. Mravlje, Strong correlations from Hund's coupling, *Annu. Rev. Condens. Matter Phys.* **4**, 137 (2013).
- [24] L. de' Medici, Hund's coupling and its key role in tuning multiorbital correlations, *Phys. Rev. B* **83**, 205112 (2011).
- [25] L. de' Medici, J. Mravlje, and A. Georges, Janus-faced influence of Hund's rule coupling in strongly correlated materials, *Phys. Rev. Lett.* **107**, 256401 (2011).
- [26] L. de' Medici, Hund's induced Fermi-liquid instabilities and enhanced quasiparticle interactions, *Phys. Rev. Lett.* **118**, 167003 (2017).
- [27] P. Werner, E. Gull, M. Troyer, and A. J. Millis, Spin freezing transition and non-Fermi-liquid self-energy in a three-orbital model, *Phys. Rev. Lett.* **101**, 166405 (2008).
- [28] K. Haule and G. Kotliar, Coherence–incoherence crossover in the normal state of iron oxypnictides and importance of Hund's rule coupling, *New J. Phys.* **11**, 025021 (2009).
- [29] S. Y. Savrasov, K. Haule, and G. Kotliar, Many-body electronic structure of americium metal, *Phys. Rev. Lett.* **96**, 036404 (2006).
- [30] J. H. Shim, K. Haule, and G. Kotliar, Fluctuating valence in a correlated solid and the anomalous properties of δ -plutonium, *Nature (London)* **446**, 513 (2007).
- [31] M. Janoschek, P. Das, B. Chakrabarti, D. L. Abernathy, M. D. Lumsden, J. M. Lawrence, J. D. Thompson, G. H. Lander, J. N. Mitchell, S. Richmond, M. Ramos, F. Trouw, J.-X. Zhu, K. Haule, G. Kotliar, and E. D. Bauer, The valence-fluctuating ground state of plutonium, *Sci. Adv.* **1**, e1500188 (2015).
- [32] M. C. Gutzwiller, Effect of correlation on the ferromagnetism of transition metals, *Phys. Rev. Lett.* **10**, 159 (1963).
- [33] M. C. Gutzwiller, Effect of correlation on the ferromagnetism of transition metals, *Phys. Rev.* **134**, A923 (1964).
- [34] W. Metzner and D. Vollhardt, Correlated lattice fermions in $d = \infty$ dimensions, *Phys. Rev. Lett.* **62**, 324 (1989).
- [35] J. Bünemann, W. Weber, and F. Gebhard, Multiband Gutzwiller wave functions for general on-site interactions, *Phys. Rev. B* **57**, 6896 (1998).
- [36] J. Bünemann and F. Gebhard, Equivalence of Gutzwiller and slave-boson mean-field theories for multiband Hubbard models, *Phys. Rev. B* **76**, 193104 (2007).
- [37] M. Fabrizio, Gutzwiller description of non-magnetic Mott insulators: Dimer lattice model, *Phys. Rev. B* **76**, 165110 (2007).
- [38] N. Lanatà, P. Barone, and M. Fabrizio, Fermi-surface evolution across the magnetic phase transition in the Kondo lattice model, *Phys. Rev. B* **78**, 155127 (2008).
- [39] N. Lanatà, H. U. R. Strand, X. Dai, and B. Hellsing, Efficient implementation of the Gutzwiller variational method, *Phys. Rev. B* **85**, 035133 (2012).
- [40] J. I. Facio, J. Mravlje, L. Pourovskii, P. S. Cornaglia, and V. Vildosola, Spin-orbit and anisotropic strain effects on the electronic correlations in Sr_2RuO_4 , *Phys. Rev. B* **98**, 085121 (2018).
- [41] F. Lechermann, A. Georges, G. Kotliar, and O. Parcollet, Rotationally invariant slave-boson formalism and momentum dependence of the quasiparticle weight, *Phys. Rev. B* **76**, 155102 (2007).
- [42] N. Lanatà, Y. Yao, X. Deng, V. Dobrosavljević, and G. Kotliar, Slave boson theory of orbital differentiation with crystal field effects: Application to UO_2 , *Phys. Rev. Lett.* **118**, 126401 (2017).
- [43] K. M. Ho, J. Schmalian, and C. Z. Wang, Gutzwiller density functional theory for correlated electron systems, *Phys. Rev. B* **77**, 073101 (2008).
- [44] X. Deng, X. Dai, and Z. Fang, LDA+Gutzwiller method for correlated electron systems, *Europhys. Lett.* **83**, 37008 (2008).
- [45] X. Deng, L. Wang, X. Dai, and Z. Fang, Local density approximation combined with Gutzwiller method for correlated electron systems: Formalism and applications, *Phys. Rev. B* **79**, 075114 (2009).
- [46] Y. X. Yao, J. Schmalian, C. Z. Wang, K. M. Ho, and G. Kotliar, Comparative study of the electronic and magnetic properties of $BaFe_2As_2$ and $BaMn_2As_2$ using the Gutzwiller approximation, *Phys. Rev. B* **84**, 245112 (2011).
- [47] Y. X. Yao, C. Z. Wang, and K. M. Ho, Including many-body screening into self-consistent calculations: Tight-binding model studies with the Gutzwiller approximation, *Phys. Rev. B* **83**, 245139 (2011).
- [48] C. Piefke and F. Lechermann, LDA+slave-boson approach to the correlated electronic structure of the metamagnetic bilayer ruthenate $Sr_3Ru_2O_7$, *Physica Status Solidi B* **248**, 2269 (2011).
- [49] N. Lanatà, Y.-X. Yao, C.-Z. Wang, K.-M. Ho, J. Schmalian, K. Haule, and G. Kotliar, γ - α isostructural transition in cerium, *Phys. Rev. Lett.* **111**, 196801 (2013).
- [50] N. Lanatà, Y. Yao, C.-Z. Wang, K.-M. Ho, and G. Kotliar, Phase diagram and electronic structure of praseodymium and plutonium, *Phys. Rev. X* **5**, 011008 (2015).
- [51] N. Lanatà, Derivation of the ghost Gutzwiller approximation from quantum embedding principles: Ghost density matrix embedding theory, *Phys. Rev. B* **108**, 235112 (2023).
- [52] G. Knizia and G. K.-L. Chan, Density matrix embedding: A simple alternative to dynamical mean-field theory, *Phys. Rev. Lett.* **109**, 186404 (2012).
- [53] T. Ayral, T.-H. Lee, and G. Kotliar, Dynamical mean-field theory, density-matrix embedding theory, and rotationally invariant slave bosons: A unified perspective, *Phys. Rev. B* **96**, 235139 (2017).
- [54] T.-H. Lee, T. Ayral, Y.-X. Yao, N. Lanata, and G. Kotliar, Rotationally invariant slave-boson and density matrix embedding theory: Unified framework and comparative study on the one-dimensional and two-dimensional Hubbard model, *Phys. Rev. B* **99**, 115129 (2019).
- [55] M. S. Frank, T.-H. Lee, G. Bhattacharyya, P. K. H. Tsang, V. L. Quito, V. Dobrosavljević, O. Christiansen, and N. Lanatà, Quantum embedding description of the Anderson lattice model with the ghost Gutzwiller approximation, *Phys. Rev. B* **104**, L081103 (2021).
- [56] N. Lanatà, T.-H. Lee, Y.-X. Yao, V. Stevanović, and V. Dobrosavljević, Connection between Mott physics and crystal structure in a series of transition metal binary compounds, *npj Comput. Mater.* **5**, 30 (2019).

- [57] N. Lanatà, T.-H. Lee, Y.-X. Yao, and V. Dobrosavljević, Emergent Bloch excitations in Mott matter, *Phys. Rev. B* **96**, 195126 (2017).
- [58] N. Lanatà, Operatorial formulation of the ghost rotationally invariant slave-boson theory, *Phys. Rev. B* **105**, 045111 (2022).
- [59] T.-H. Lee, N. Lanatà, and G. Kotliar, Accuracy of ghost rotationally invariant slave-boson and dynamical mean field theory as a function of the impurity-model bath size, *Phys. Rev. B* **107**, L121104 (2023).
- [60] D. Guerci, M. Capone, and M. Fabrizio, Exciton Mott transition revisited, *Phys. Rev. Mater.* **3**, 054605 (2019).
- [61] C. Mejuto-Zaera and M. Fabrizio, Efficient computational screening of strongly correlated materials: Multiorbital phenomenology within the ghost Gutzwiller approximation, *Phys. Rev. B* **107**, 235150 (2023).
- [62] T.-H. Lee, C. Melnick, R. Adler, N. Lanatà, and G. Kotliar, Accuracy of ghost-rotationally-invariant slave-boson theory for multiorbital Hubbard models and realistic materials, *Phys. Rev. B* **108**, 245147 (2023).
- [63] D. Guerci, Beyond simple variational approach for strongly correlated electron systems, Ph.D. thesis, International School for Advanced Studies, 2019.
- [64] M. Caffarel and W. Krauth, Exact diagonalization approach to correlated fermions in infinite dimensions: Mott transition and superconductivity, *Phys. Rev. Lett.* **72**, 1545 (1994).
- [65] S. R. White, Density matrix formulation for quantum renormalization groups, *Phys. Rev. Lett.* **69**, 2863 (1992).
- [66] S. R. White, Density-matrix algorithms for quantum renormalization groups, *Phys. Rev. B* **48**, 10345 (1993).
- [67] U. Schollwöck, The density-matrix renormalization group, *Rev. Mod. Phys.* **77**, 259 (2005).
- [68] J. Rogers, T.-H. Lee, S. Pakdel, W. Xu, V. Dobrosavljević, Y.-X. Yao, O. Christiansen, and N. Lanatà, Bypassing the computational bottleneck of quantum-embedding theories for strong electron correlations with machine learning, *Phys. Rev. Res.* **3**, 013101 (2021).
- [69] M. S. Frank, D. G. Artiukhin, T.-H. Lee, Y. Yao, K. Barros, O. Christiansen, and N. Lanatà, Active learning approach to simulations of strongly correlated matter with the ghost Gutzwiller approximation, *Phys. Rev. Res.* **6**, 013242 (2024).
- [70] O. K. Andersen, Linear methods in band theory, *Phys. Rev. B* **12**, 3060 (1975).
- [71] P. Blaha, K. Schwarz, F. Tran, R. Laskowski, G. K. H. Madsen, and L. D. Marks, WIEN2k: An APW+lo program for calculating the properties of solids, *J. Chem. Phys.* **152**, 074101 (2020).
- [72] Y.-X. Yao, N. Lanatà, C.-Z. Wang, K.-M. Ho, and G. Kotliar, Gutzwiller variational embedding simulation package (CyGutz), <https://doi.org/10.6084/m9.figshare.11987439>.
- [73] H. Zhai, H. R. Larsson, S. Lee, Z.-H. Cui, T. Zhu, C. Sun, L. Peng, R. Peng, K. Liao, J. Tölle, J. Yang, S. Li, and G. K.-L. Chan, Block2: A comprehensive open source framework to develop and apply state-of-the-art DMRG algorithms in electronic structure and beyond, *J. Chem. Phys.* **159**, 234801 (2023).
- [74] M. J. Rey, P. Dehadt, J. C. Joubert, B. Lambert-Andron, M. Cyrot, and F. Cyrot-Lackmann, Preparation and structure of the compounds SrVO_3 and Sr_2VO_4 , *J. Solid State Chem.* **86**, 101 (1990).
- [75] A. Fujimori, I. Hase, H. Namatame, Y. Fujishima, Y. Tokura, H. Eisaki, S. Uchida, K. Takegahara, and F. M. F. de Groot, Evolution of the spectral function in Mott-Hubbard systems with d^1 configuration, *Phys. Rev. Lett.* **69**, 1796 (1992).
- [76] I. H. Inoue, I. Hase, Y. Aiura, A. Fujimori, Y. Haruyama, T. Maruyama, and Y. Nishihara, Systematic development of the spectral function in the $3d^1$ Mott-Hubbard system $\text{Ca}_{1-x}\text{Sr}_x\text{VO}_3$, *Phys. Rev. Lett.* **74**, 2539 (1995).
- [77] K. Yoshimatsu, T. Okabe, H. Kumigashira, S. Okamoto, S. Aizaki, A. Fujimori, and M. Oshima, Dimensional-crossover-driven metal-insulator transition in SrVO_3 ultrathin films, *Phys. Rev. Lett.* **104**, 147601 (2010).
- [78] A. Liebsch, Surface versus bulk Coulomb correlations in photoemission spectra of SrVO_3 and CaVO_3 , *Phys. Rev. Lett.* **90**, 096401 (2003).
- [79] A. Sekiyama, H. Fujiwara, S. Imada, S. Suga, H. Eisaki, S. I. Uchida, K. Takegahara, H. Harima, Y. Saitoh, I. A. Nekrasov, G. Keller, D. E. Kondakov, A. V. Kozhevnikov, Th. Pruschke, K. Held, D. Vollhardt, and V. I. Anisimov, Mutual experimental and theoretical validation of bulk photoemission spectra of $\text{Sr}_{1-x}\text{Ca}_x\text{VO}_3$, *Phys. Rev. Lett.* **93**, 156402 (2004).
- [80] T. Yoshida, K. Tanaka, H. Yagi, A. Ino, H. Eisaki, A. Fujimori, and Z.-X. Shen, Direct observation of the mass renormalization in SrVO_3 by angle resolved photoemission spectroscopy, *Phys. Rev. Lett.* **95**, 146404 (2005).
- [81] I. A. Nekrasov, K. Held, G. Keller, D. E. Kondakov, Th. Pruschke, M. Kollar, O. K. Andersen, V. I. Anisimov, and D. Vollhardt, Momentum-resolved spectral functions of SrVO_3 calculated by LDA + DMFT, *Phys. Rev. B* **73**, 155112 (2006).
- [82] J. M. Tomczak, M. Casula, T. Miyake, F. Aryasetiawan, and S. Biermann, Combined GW and dynamical mean-field theory: Dynamical screening effects in transition metal oxides, *Europhys. Lett.* **100**, 67001 (2012).
- [83] C. Taranto, M. Kaltak, N. Parragh, G. Sangiovanni, G. Kresse, A. Toschi, and K. Held, Comparing quasiparticle GW+DMFT and LDA+DMFT for the test bed material SrVO_3 , *Phys. Rev. B* **88**, 165119 (2013).
- [84] J. M. Tomczak, M. Casula, T. Miyake, and S. Biermann, Asymmetry in band widening and quasiparticle lifetimes in SrVO_3 : Competition between screened exchange and local correlations from combined GW and dynamical mean-field theory GW + DMFT, *Phys. Rev. B* **90**, 165138 (2014).
- [85] K. Haule, T. Birol, and G. Kotliar, Covalency in transition-metal oxides within all-electron dynamical mean-field theory, *Phys. Rev. B* **90**, 075136 (2014).
- [86] K. Haule and T. Birol, Free energy from stationary implementation of the DFT + DMFT functional, *Phys. Rev. Lett.* **115**, 256402 (2015).
- [87] Z. Zhong, M. Wallerberger, J. M. Tomczak, C. Taranto, N. Parragh, A. Toschi, G. Sangiovanni, and K. Held, Electronics with correlated oxides: $\text{SrVO}_3/\text{SrTiO}_3$ as a Mott transistor, *Phys. Rev. Lett.* **114**, 246401 (2015).
- [88] A. Paul and T. Birol, Strain tuning of plasma frequency in vanadate, niobate, and molybdate perovskite oxides, *Phys. Rev. Mater.* **3**, 085001 (2019).
- [89] A. D. N. James, M. Aichhorn, and J. Laverock, Quantum confinement induced metal-insulator transition in strongly correlated quantum wells of SrVO_3 superlattices, *Phys. Rev. Res.* **3**, 023149 (2021).

- [90] M. Pickem, J. Kaufmann, K. Held, and J. M. Tomczak, Zoology of spin and orbital fluctuations in ultrathin oxide films, *Phys. Rev. B* **104**, 024307 (2021).
- [91] G. A. Sawatzky and J. W. Allen, Magnitude and origin of the band gap in NiO, *Phys. Rev. Lett.* **53**, 2339 (1984).
- [92] W. Jauch and M. Reehuis, Electron density distribution in paramagnetic and antiferromagnetic nio: A γ -ray diffraction study, *Phys. Rev. B* **70**, 195121 (2004).
- [93] J. Zaanen, G. A. Sawatzky, and J. W. Allen, Band gaps and electronic structure of transition-metal compounds, *Phys. Rev. Lett.* **55**, 418 (1985).
- [94] A. Fujimori and F. Minami, Valence-band photoemission and optical absorption in nickel compounds, *Phys. Rev. B* **30**, 957 (1984).
- [95] F. C. Zhang and T. M. Rice, Effective Hamiltonian for the superconducting Cu oxides, *Phys. Rev. B* **37**, 3759 (1988).
- [96] J. Bała, A. M. Oleś, and J. Zaanen, Zhang-Rice localization, quasiparticle dispersions, and the photoemission of NiO, *Phys. Rev. Lett.* **72**, 2600 (1994).
- [97] J. Kuneš, V. I. Anisimov, S. L. Skornyakov, A. V. Lukoyanov, and D. Vollhardt, NiO: Correlated band structure of a charge-transfer insulator, *Phys. Rev. Lett.* **99**, 156404 (2007).
- [98] M. Taguchi, M. Matsunami, Y. Ishida, R. Eguchi, A. Chainani, Y. Takata, M. Yabashi, K. Tamasaku, Y. Nishino, T. Ishikawa, Y. Senba, H. Ohashi, and S. Shin, Revisiting the valence-band and core-level photoemission spectra of NiO, *Phys. Rev. Lett.* **100**, 206401 (2008).
- [99] Q. Yin, A. Gordienko, X. Wan, and S. Y. Savrasov, Calculated momentum dependence of Zhang-Rice states in transition metal oxides, *Phys. Rev. Lett.* **100**, 066406 (2008).
- [100] J. Kuneš, V. I. Anisimov, A. V. Lukoyanov, and D. Vollhardt, Local correlations and hole doping in NiO: A dynamical mean-field study, *Phys. Rev. B* **75**, 165115 (2007).
- [101] L. Zhang, P. Staar, A. Kozhevnikov, Y.-P. Wang, J. Trinastic, T. Schulthess, and H.-P. Cheng, DFT + DMFT calculations of the complex band and tunneling behavior for the transition metal monoxides MnO, FeO, CoO, and NiO, *Phys. Rev. B* **100**, 035104 (2019).
- [102] I. Leonov, L. Pourovskii, A. Georges, and I. A. Abrikosov, Magnetic collapse and the behavior of transition metal oxides at high pressure, *Phys. Rev. B* **94**, 155135 (2016).
- [103] S. Mandal, K. Haule, K. M. Rabe, and D. Vanderbilt, Systematic beyond-DFT study of binary transition metal oxides, *npj Comput. Mater.* **5**, 115 (2019).
- [104] S. Mandal, K. Haule, K. M. Rabe, and D. Vanderbilt, Influence of magnetic ordering on the spectral properties of binary transition metal oxides, *Phys. Rev. B* **100**, 245109 (2019).
- [105] I. Leonov, A. O. Shorikov, V. I. Anisimov, and I. A. Abrikosov, Emergence of quantum critical charge and spin-state fluctuations near the pressure-induced Mott transition in MnO, FeO, CoO, and NiO, *Phys. Rev. B* **101**, 245144 (2020).
- [106] M. Karolak, G. Ulm, T. Wehling, V. Mazurenko, A. Poteryaev, and A. Lichtenstein, Double counting in LDA+DMFT—The example of NiO, *J. Electron Spectrosc. Relat. Phenom.* **181**, 11 (2010), proceedings of International Workshop on Strong Correlations and Angle-Resolved Photoemission Spectroscopy 2009.
- [107] T. Zhu, Z.-H. Cui, and G. K.-L. Chan, Efficient formulation of *ab initio* quantum embedding in periodic systems: Dynamical mean-field theory, *J. Chem. Theory Comput.* **16**, 141 (2020).
- [108] V. I. Anisimov, J. Zaanen, and O. K. Andersen, Band theory and Mott insulators: Hubbard U instead of Stoner I, *Phys. Rev. B* **44**, 943 (1991).
- [109] L. F. Mattheiss, Electronic structure of the 3d transition-metal monoxides. I. energy-band results, *Phys. Rev. B* **5**, 290 (1972).
- [110] E. v. Oelsen, G. Seibold, and J. Bünenmann, Time-dependent Gutzwiller theory for multiband Hubbard models, *Phys. Rev. Lett.* **107**, 076402 (2011).
- [111] T.-H. Lee, N. Lanatà, M. Kim, and G. Kotliar, Efficient slave-boson approach for multiorbital two-particle response functions and superconductivity, *Phys. Rev. X* **11**, 041040 (2021).
- [112] M. Schiró and M. Fabrizio, Quantum quenches in the Hubbard model: Time-dependent mean-field theory and the role of quantum fluctuations, *Phys. Rev. B* **83**, 165105 (2011).
- [113] M. Behrmann, M. Fabrizio, and F. Lechermann, Extended dynamic Mott transition in the two-band Hubbard model out of equilibrium, *Phys. Rev. B* **88**, 035116 (2013).
- [114] M. Behrmann, A. I. Lichtenstein, M. I. Katsnelson, and F. Lechermann, Versatile approach to spin dynamics in correlated electron systems, *Phys. Rev. B* **94**, 165120 (2016).
- [115] D. Guerci, M. Capone, and N. Lanatà, Time-dependent ghost Gutzwiller nonequilibrium dynamics, *Phys. Rev. Res.* **5**, L032023 (2023).
- [116] F. Lechermann, A. Georges, A. Poteryaev, S. Biermann, M. Posternak, A. Yamasaki, and O. K. Andersen, Dynamical mean-field theory using wannier functions: A flexible route to electronic structure calculations of strongly correlated materials, *Phys. Rev. B* **74**, 125120 (2006).
- [117] M. Aichhorn, L. Pourovskii, V. Vildosola, M. Ferrero, O. Parcollet, T. Miyake, A. Georges, and S. Biermann, Dynamical mean-field theory within an augmented plane-wave framework: Assessing electronic correlations in the iron pnictide lafeaso, *Phys. Rev. B* **80**, 085101 (2009).
- [118] M. Aichhorn, L. Pourovskii, and A. Georges, Importance of electronic correlations for structural and magnetic properties of the iron pnictide superconductor LaFeAsO, *Phys. Rev. B* **84**, 054529 (2011).
- [119] O. Parcollet, M. Ferrero, T. Ayral, H. Hafermann, I. Krivenko, L. Messio, and P. Seth, TRIQS: A toolbox for research on interacting quantum systems, *Comput. Phys. Commun.* **196**, 398 (2015).
- [120] M. Aichhorn, L. Pourovskii, P. Seth, V. Vildosola, M. Zingl, O. E. Peil, X. Deng, J. Mravlje, G. J. Kraberger, C. Martins, M. Ferrero, and O. Parcollet, TRIQS/DFTTools: A TRIQS application for *ab initio* calculations of correlated materials, *Comput. Phys. Commun.* **204**, 200 (2016).
- [121] V. Singh, U. Herath, B. Wah, X. Liao, A. H. Romero, and H. Park, DMFTwDFT: An open-source code combining dynamical mean field theory with various density functional theory packages, *Comput. Phys. Commun.* **261**, 107778 (2021).
- [122] S. Beck, A. Hampel, O. Parcollet, C. Ederer, and A. Georges, Charge self-consistent electronic structure calculations with

- dynamical mean-field theory using Quantum ESPRESSO, Wannier 90 and TRIQS, *J. Phys.: Condens. Matter* **34**, 235601 (2022).
- [123] A. Grechnev, I. Di Marco, M. I. Katsnelson, A. I. Lichtenstein, J. Wills, and O. Eriksson, Theory of bulk and surface quasi-particle spectra for Fe, Co, and Ni, *Phys. Rev. B* **76**, 035107 (2007).
- [124] I. Di Marco, J. Minár, S. Chadov, M. I. Katsnelson, H. Ebert, and A. I. Lichtenstein, Correlation effects in the total energy, the bulk modulus, and the lattice constant of a transition metal: Combined local-density approximation and dynamical mean-field theory applied to Ni and Mn, *Phys. Rev. B* **79**, 115111 (2009).
- [125] O. Grånäs, I. Di Marco, P. Thunström, L. Nordström, O. Eriksson, T. Björkman, and J. M. Wills, Charge self-consistent dynamical mean-field theory based on the full-potential linear muffin-tin orbital method: Methodology and applications, *Comput. Mater. Sci.* **55**, 295 (2012).
- [126] H. Shinaoka, J. Otsuki, M. Kawamura, N. Takemori, and K. Yoshimi, DCore: Integrated DMFT software for correlated electrons, *SciPost Phys.* **10**, 117 (2021).
- [127] R. Adler, C. Melnick, and G. Kotliar, Portobello - quantum embedding in correlated materials made accessible, *Comput. Phys. Commun.* **294**, 108907 (2024).
- [128] S. Choi, P. Semon, B. Kang, A. Kutepov, and G. Kotliar, ComDMFT: A massively parallel computer package for the electronic structure of correlated-electron systems, *Comput. Phys. Commun.* **244**, 277 (2019).
- [129] B. Kang, P. Semon, C. Melnick, G. Kotliar, and S. Choi, ComDMFT v.2.0: Fully self-consistent *ab initio* GW+EDMFT for the electronic structure of correlated quantum materials, [arXiv:2310.04613](https://arxiv.org/abs/2310.04613).